Applied Surface Science 563 (2021) 150209

Contents lists available at ScienceDirect

Applied Surface Science

journal homepage: www.elsevier.com/locate/apsusc

Full Length Article

Hematite rhombuses for chemiresitive ozone sensors: Experimental and theoretical approaches

Ariadne C. Catto [a,*], Marisa C. Oliveira [a], Renan A.P. Ribeiro [b], Waldir Avansi Jr [c], Luís F. da Silva [c], Elson Longo [a]

[a] Center for the Development of Functional Materials (CDMF), Federal University of São Carlos, São Carlos, SP, Brazil
[b] Department of Chemistry, State University of Minas Gerais, Divinópolis, MG, Brazil
[c] Laboratory of Nanostructured Multifunctional Materials, Federal University of São Carlos, São Carlos, SP, Brazil

ARTICLE INFO

Keywords:
Crystal
Hematite
Hydrothermal
Chemiresistor
Ozone
DFT calculations

ABSTRACT

This manuscript addresses an experimental and theoretical investigation regarding the ozone (O_3) gas-sensing properties of hematite microrhombuses obtained via the hydrothermal method. Gas-sensing experiments showed the sensitivity of the microrhombuses towards O_3 gas from 12 ppb (parts-per-billion), presenting total recovery and a long-term stability of 4 months. Theoretical calculations revealed that the surfaces play an important role in the adsorption/desorption processes. Moreover, it was found that the presence of (1 0 4) surfaces is favorable to the high sensitivity towards O_3 molecules, confirming the experimental results. These results allowed us to better understand the morphological changes and directly relate the sensing performance of hematite microcrystals at different exposed surfaces.

1. Introduction

Air pollution is caused by the emission of certain gases and particles that constitute the atmosphere. Over time, it can cause harm to human health and/or the environment. Among the main ground-level pollutants that are the most harmful to human health – causing cardiovascular and respiratory diseases – is ozone (O_3) gas, an environmental air pollutant with high potential for toxicity [1–3]. Therefore, it needs precise detection to make sure its concentration is below 120 ppb (parts-per-billion). Up to now, several researchers have made unremitting efforts to develop sensors exhibiting high sensitivity, reproducibility and long-time stability, besides working at relatively low temperatures [4–6].

Metal semiconducting oxides (MOXs) have been widely employed in gas sensors due to their potential features, such as high-sensitivity, selectivity, rapid gas detection, and stability. The n-type MOXs (e.g. SnO_2, WO_3, In_2O_3, ZnO, and α-Fe_2O_3) have been used as chemiresistors for the detection of reducing and oxidizing analytes [7–9]. Several studies have demonstrated the potential of MOXs as ozone gas-sensing layer [4,5,10,11]. Likewise, our research team has been encouraged to fabricate MOXs-based gas sensors focused mainly on the detection of O_3, such as $Co_xZn_{1-x}O$, ZnO, ZnO/SnO_2, $ZnFe_2O_4$, α-Ag_2WO_4, $CuWO_4$ and V_2O_5/TiO_2 [12–18]. Among them, we propose an ozone gas sensor based on $Co_xZn_{1-x}O$ thin films which showed good response when exposed to 84 ppb of O_3 gas at an operating temperature of 200 °C. Compared with the pristine ZnO, the Co-doped ZnO sample exhibited a higher response (ca. 5 times) and overcame poor selectivity shortcoming. This enhanced sensor response of the fabricated sensor was ascribed to the catalytic role of the doped Co and the increase of oxygen vacancies [14].

Multiple factors behind gas-sensing properties have been considered responsible for improving sensor performance, including crystalline structure, morphological characteristics, crystallization degree, among others [16,19,20]. Another important aspect to consider is the relationship between sensing performance and MOX exposed facets/surfaces. In this sense, Gurlo reported the importance of the MOX crystal shape in its gas-sensing performance. According to the author, the nature of surfaces exposed to the target gas becomes a key factor to enhance the material sensing activity, as some facets exhibit higher reactivity to certain analytes than other surfaces [21].

Hematite (α-Fe_2O_3) exhibits a corundum-type crystal structure with R_3c rhombohedral space group, in which the oxygen O^{2-} ions are arranged in a hexagonal close-packed structure with two-thirds of octahedral interstices filled with trivalent Fe. This arrangement forms FeO_6

* Corresponding author.
E-mail address: ade.catto@gmail.com (A.C. Catto).

https://doi.org/10.1016/j.apsusc.2021.150209
Received 29 March 2021; Received in revised form 4 May 2021; Accepted 22 May 2021
Available online 5 June 2021

octahedra, which consist of the central Fe^{3+} cation and the surrounding anion ligands, being considered the most stable iron oxide with n-type semiconducting properties ($E_g = 2.1$ eV at 300 K) [22,23].

Previous studies have mainly focused on α-Fe_2O_3 materials, which have demonstrated remarkable catalytic properties due to the high oxygen ion mobility at the material surface [22]. In terms of gas-sensing applications, a few studies have recently demonstrated the applicability of Fe_2O_3 compound for the detection of formaldehyde (HCHO), H_2, CO, and NH_3 [24–26]. For example, Umar et al. prepared a cubic-shaped hematite microstructure for application as a gas-sensing layer. They observed a high response at 400 °C towards ethanol in comparison with other analytes, i.e., H_2 and CO gases [27].

Recently, we reported the promising application of hematite microrhombuses as a sensing material to manufacture BTEX (benzene, toluene, ethylbenzene, and xylenes) gas sensor devices [9]. By analyzing the response of the sensor exposed to a wide variety of organic compounds and BTEX gases, we found that hematite microrhombuses exhibited a good selectivity to BTEX gases compared to the investigated VOC gases, in addition to remarkable sensing properties with excellent repeatability and long-term stability, even at low-gas levels [9]. Although the surface structure-dependent sensing properties are well recognized, the experimental-theoretical study applying hematite crystals as an ozone gas-sensing layer is still lacking.

The density functional theory (DFT) study has been a useful tool to support the experimental approach, providing an in-depth understanding of the surface–adsorbate interaction [28,29]. By performing DFT calculations, Wei et al. [30] examined the adsorption of NH_3 molecules on Co_3O_4 hexagonal platelets exposed by (1 1 2) crystal plane. The theoretical results revealed that the high percentage of high-energy (1 1 2) facets of Co_3O_4 platelets could be enhanced in order to obtain more efficiency in the monitoring of NH_3 gas, which is consistent with experimental conclusions. Moreover, the authors proposed that DFT calculations can be used to evaluate the selectivity of gas sensors by designing special crystal-facet exposure [30]. Likewise, Wang and coworkers [31] demonstrated through DFT calculations that a high proportion of reactive NiO (1 1 0) facets could act synergistically to promote the selective response to CO adsorption [31]. Recently, we successfully combined experimental and DFT calculations to understand the role of shape-oriented $ZnFe_2O_4$ nanoparticles in O_3 gas-sensing properties, confirming that the chemical environment along the exposed surfaces can be responsible for selectivity, reversibility and spontaneity factors of the different adsorption mechanisms [13].

Motivated by these arguments, we report the first comprehensive experimental-theoretical study regarding the role played by exposed surfaces of hematite microcrystals in the sensing properties towards O_3 gas. The microstructural and surface properties of the as-prepared hematite crystals were investigated experimentally. Electrical measurements revealed good sensitivity, repeatability, and stability of the hematite crystals applied in the detection of sub-ppm levels of O_3 gas. Furthermore, the electronic properties of the adsorption systems discussed in view of the projected density of states, confirm that high-energy crystal facets of hematite crystals have a high activity for monitoring the O_3 molecules. The findings of this work provide a useful experimental/theoretical reference for the rational development of efficient gas sensors based on hematite crystals.

2. Experimental section

2.1. Synthesis of the hematite crystals

Rhombus-like hematite powders were synthesized via the hydrothermal treatment, as reported in ref. 9. Both iron (III) chloride ($FeCl_3{\cdot}6H_2O$, 99.9%) and ethyl alcohol anhydrous (CH_3CH_2OH, 99.5%) purchased from Sigma-Aldrich Corporation were used in the synthesis procedure. First, $FeCl_3$ (0.06 M) was added to 100 mL of ethyl alcohol under constant stirring at room temperature. Afterwards, 22.5 mL of deionized water was slowly dropped into the iron reactional solution, which was then kept under stirring for 30 min. The dialysis process was applied to remove the chloride, and the obtained precipitate was dried in an electric oven at 80 °C overnight. To obtain the pristine hematite phase, 100 mg of the precipitate was added to 100 mL of deionized water, being then treated in a hydrothermal system at 200 °C for 4 h at a heating rate of 2 °C.min^{-1}. At the end of the hydrothermal treatment, the as-obtained powder was washed with deionized water and isopropyl alcohol and dried in an electric oven at 80 °C overnight under air atmosphere.

2.2. Characterization techniques

The sample was characterized by X-ray diffraction measurements (Rigaku diffractometer, D/Max-2500PC, CuKα radiation) in a 2θ range from 20° to 80° with a step of 0.02, and at a scanning speed of 2° min^{-1}. Ultraviolet–visible diffuse reflectance spectrum (UV–Vis DRS) was collected using a spectrophotometer (Shimadzu, UV-2600) coupled to an integrating sphere from 350 to 700 nm. The optical gap (E_g) value was estimated using the Kubelka-Munk function [32]. The morphological features were investigated using a field emission scanning electron microscope (FE-SEM, Zeiss Supra35) and a high-resolution transmission electron microscope (HRTEM, FEI Tecnai G2 F20) operated at 200 KeV. The average particle size was estimated from FE-SEM images using approximately 100 particles. The chemical and surface analyses were conducted in an X-ray photoelectron spectrometer (XPS; Thermo Scientific K-Alpha) using a monochromatic AlKα X-ray source. The spectrum had its peak fitted using Casa XPS software, and all binding energies were given with reference to the C 1 s signal (284.8 eV) arising from the surface hydrocarbons.

2.3. Sensing experiments

To perform the ozone gas-sensing measurements, the sensor sample was prepared following the procedure adopted by our team [11,12,33]. Hematite powders (50 mg) were dispersed in 0.5 mL of isopropyl alcohol using an ultrasonic cleaner for 30 min. Afterwards, the suspension was dripped onto a SiO_2/Si substrate with 120 nm thick Pt electrodes separated by a distance of 50 mm. The sensor sample was annealed at 500 °C for 30 min at a heating rate of 5 °C.min^{-1}. Details regarding the electrode preparation as well as the gas-sensing workbench used here for ozone sensing experiments can be found elsewhere [34]. The sensor sample was inserted into a special chamber that allows the control of the substrate temperature, gas flows and O_3 levels. The O_3 gas was generated from oxidizing oxygen molecules of the dry air using a calibrated pen-ray UV lamp (model P/N 90–0004-01), providing gas concentrations from 12 to 550 ppb (parts-per-billion). In these dynamic experiments, the dry air (carrier gas) containing O_3 gas was blown directly onto the sample. The electrical resistance of the sample was monitored using a Keithley electrometer (model 6514) with a dc voltage of 1 V. The sensor response (S) was defined as $S = R_{O3}/R_{air}$, where R_{O3} and R_{air} are the electric resistance of the sensor exposed to O_3 gas and dry air, respectively. In addition, the response time was defined as the period required for the sample electrical resistance to reach 90% of its initial value when exposed to the target gas. Similarly, the recovery time was defined as the time required for the sensor electrical resistance to recover 90% of its initial value after the ozone gas is turned off. To determine the long-term stability over a period of 4 months, the sample was stored and exposed to 20 ppb of ozone gas at a working temperature of 150 °C every amount of days by measuring the repeated adsorption/desorption cycles. In the gas-sensing experiments, at least 3 exposure cycles were collected to ensure the reliability of the sensor response.

2.4. Computational methods and periodic models

In order to corroborate the experimental results for Fe_2O_3

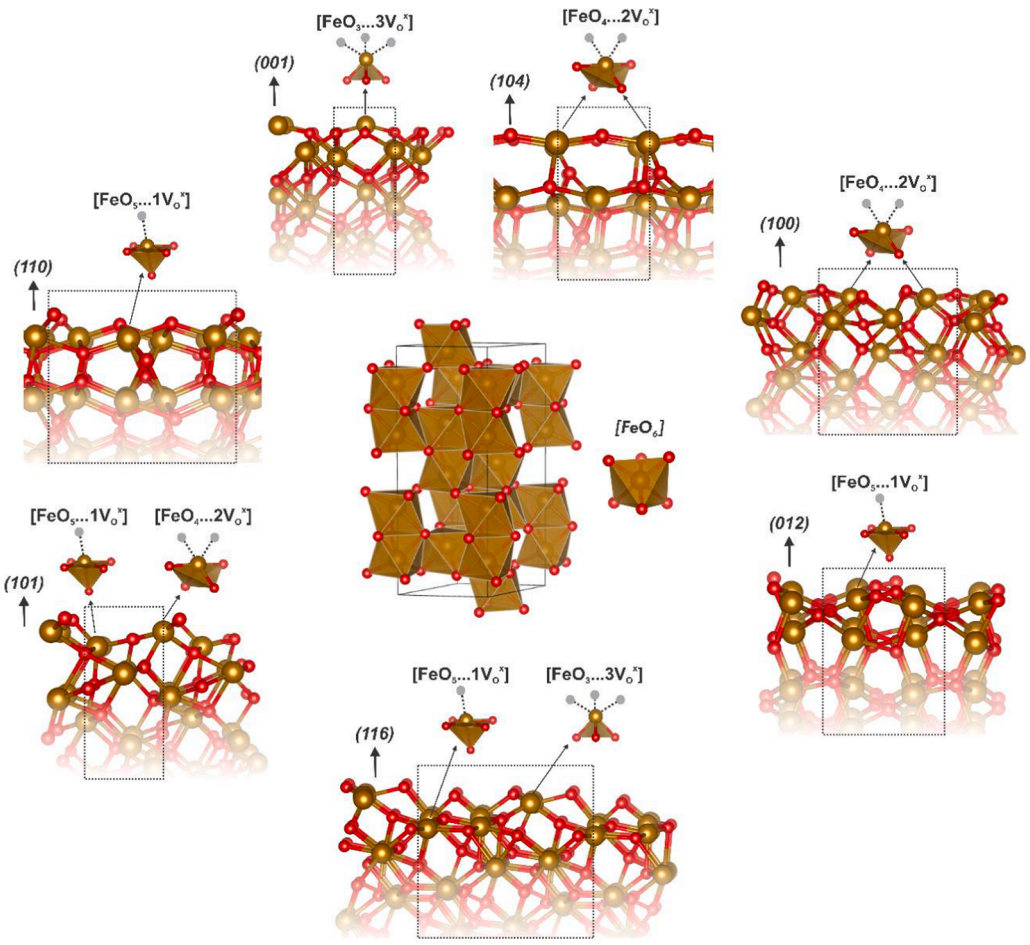

Fig. 1. Schematic representation of the conventional unit cell for hematite crystal (center panel) depicting the [FeO_6] cluster environment. The (0 0 1), (1 0 0), (1 0 1), (1 1 0), (0 1 2), (1 0 4) and (1 1 6) surfaces were depicted highlighting the exposed clusters. Brown and red balls correspond to Fe and O atoms, respectively. (For interpretation of the references to colour in this figure legend, the reader is referred to the web version of this article.)

microcrystals, quantum–mechanical calculations in the framework of the density functional theory (DFT) were carried out using B3LYP-D3 [35,36] exchange correlation functional augmented with two- and three-body contributions to the long-range dispersion energy (Grimme D3), as implemented in CRYSTAL17 code [37]. In this work, the crystalline structure of hematite (α-Fe_2O_3) was built based on Rietveld refinement experimental results.

The Fe and O atoms were described by atom-centered all-electron basis set defined as 86-411d41G and 8-411G*, respectively [38]. The crystalline structure was fully relaxed (atomic positions and lattice parameters) as a function of the total energy, and the electronic integration over the BZ was performed using a $6 \times 6 \times 6$ Monkhorst–Pack *k*-mesh [39]. Five thresholds were set to 8, 8, 8, 8, and 14 in order to control the accuracy of the Coulomb and exchange integral calculations. The convergence criteria for mono and bielectronic integrals was set to 10^{-8} Hartree, while the RMS gradient, RMS displacement, maximum gradient and maximum displacement were set to 3×10^{-4}, 1.2×10^{-3}, 4.5×10^{-4} and 1.8×10^{-3} a.u., respectively. The electronic properties were evaluated through density of states (DOS), band structure profiles and charge analysis tools implemented in the CRYSTAL17 code [37].

Concerning the magnetic ground state for α-Fe_2O_3 two collinear magnetic configurations were considered using the primitive unit cell: ferromagnetic (FEM) and antiferromagnetic (AFM). The magnetic ground state was defined as an AFM model (↑↓↓↑) according to the energy difference between the models, following previous theoretical and experimental results [40].

To get a deep insight into the structural and electronic properties of hematite surfaces, DFT calculations were carried out for (0 0 1), (1 0 0), (1 0 1), (1 1 0), (0 1 2), (1 0 4) and (1 1 6) surfaces, as depicted in Fig. 1, following previous theoretical and experimental studies [41]. Herein, the magnetic ordering was defined based on the AFM arrangement previously selected for the bulk α-Fe_2O_3 model. Moreover, it is important to point out that the CRYSTAL17 code is based on the linear combination of localized Gaussian basis functions. Therefore, the surface-based calculations do not require a finite vacuum space to be defined [42,43].

Once symmetric and stoichiometric slabs were considered, the surface energy (E_{surf}) was calculated following the expression:

$$\mathbf{E_{surf}} = \frac{(\mathbf{E_{slab}} - \mathbf{nE_{bulk}})}{\mathbf{2A}} \quad (1)$$

where E_{slab} and E_{bulk} correspond to the total energy of slab and bulk models, respectively, n is the number of bulk units in the slab and A is the surface area for symmetric slabs.

The equilibrium shape of a crystal and its modulations can be calculated from the Wulff construction, which minimizes the total surface free energy at a fixed volume, providing a simple relationship between the surface energy (E_{surf}) of a (*hkl*) plane and its distance from the crystallite center in the normal direction [44,45]. Therefore, by combining the calculated E_{surf} values for different hematite surfaces it is possible to compare the morphological modulations of hematite crystals

and the experimental findings according to previous studies and references therein [45-49].

Furthermore, to investigate the role of hematite surfaces in the O_3 sensing properties, adsorption models were constructed from (2 × 1) supercell expansions of previously optimized slabs. The adsorption enthalpy was calculated considering the expression:

$$E_{ads} = \frac{1}{N}[E_{(slab+O_3)} - (E_{slab} + NE_{O_3}) + E_{BSSE}] \quad (2)$$

where, $E_{(slab+O_3)}$ is the total energy of the optimized slab with adsorbed O_3 molecule, E_{slab} is the total energy of the isolated optimized slab, N is the number of adsorbed O_3 molecules per unit cell and E_{O_3} is the total energy of ozone in the gas phase.

The basis set superposition error (BSSE) was calculated following the expression [50]:

$$E_{BSSE} = \left(E^{frozen}_{slab} - E^{frozen}_{slab+ghost}\right) + \left(E^{frozen}_{O_3} - E^{frozen}_{O_3+ghost}\right) \quad (3)$$

where all the energies refer to the geometries of the two separated moieties (slab + O_3) frozen in the minimum adsorption configuration, with and without ghost functions.

3. Results and discussion

3.1. Microstructural and surface properties

The X-ray diffraction pattern and absorbance spectrum of the as-prepared hematite sample are shown in Fig. 2 (a) and **Fig S1**. According to Fig. 2**(a)**, all reflections were indexed to the hematite crystalline phase with rhombohedral structure (JCPDS card No. 87–1164). From **Fig. S1**, it was possible to obtain an optical gap (E_g) value of approximately 2.1 eV, which is in agreement with reported data for pristine hematite [51–53]. The SEM and TEM analysis, Fig. 2 (b, c), as expected [9,22], revealed that the as-obtained sample is based on well-defined crystals with a rhombus-like shape of an average size of 1.4 μm. The HR-TEM image of the region of an individual crystal, Fig. 2**(d)**, shows the monocrystalline nature of the hematite rhombus, with the (1 0 4) crystallographic plane being related to the hematite phase, which is in accordance with our previous work [9].

The chemical composition and electronic state of surface that constitute the species were analyzed by XPS technique to get insights into the gas-sensing performance of the hematite crystals. As displayed in Fig. 3**(a)**, the XPS survey spectrum of the as-prepared sample reveals

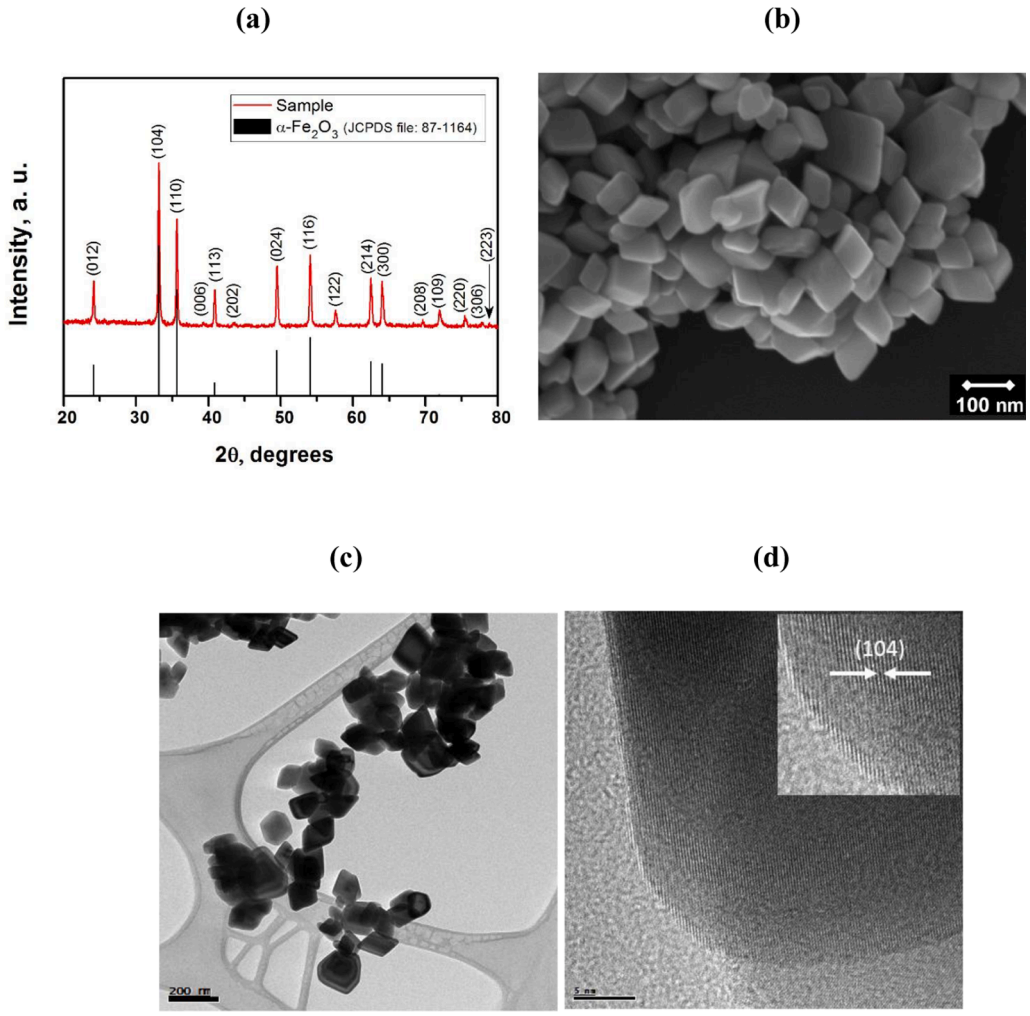

Fig. 2. Rhombus-like shape α-Fe_2O_3 crystals: (a) XRD pattern, and (b) SEM image, (c) TEM image; and (d) HRTEM images of the selected nanoparticle.

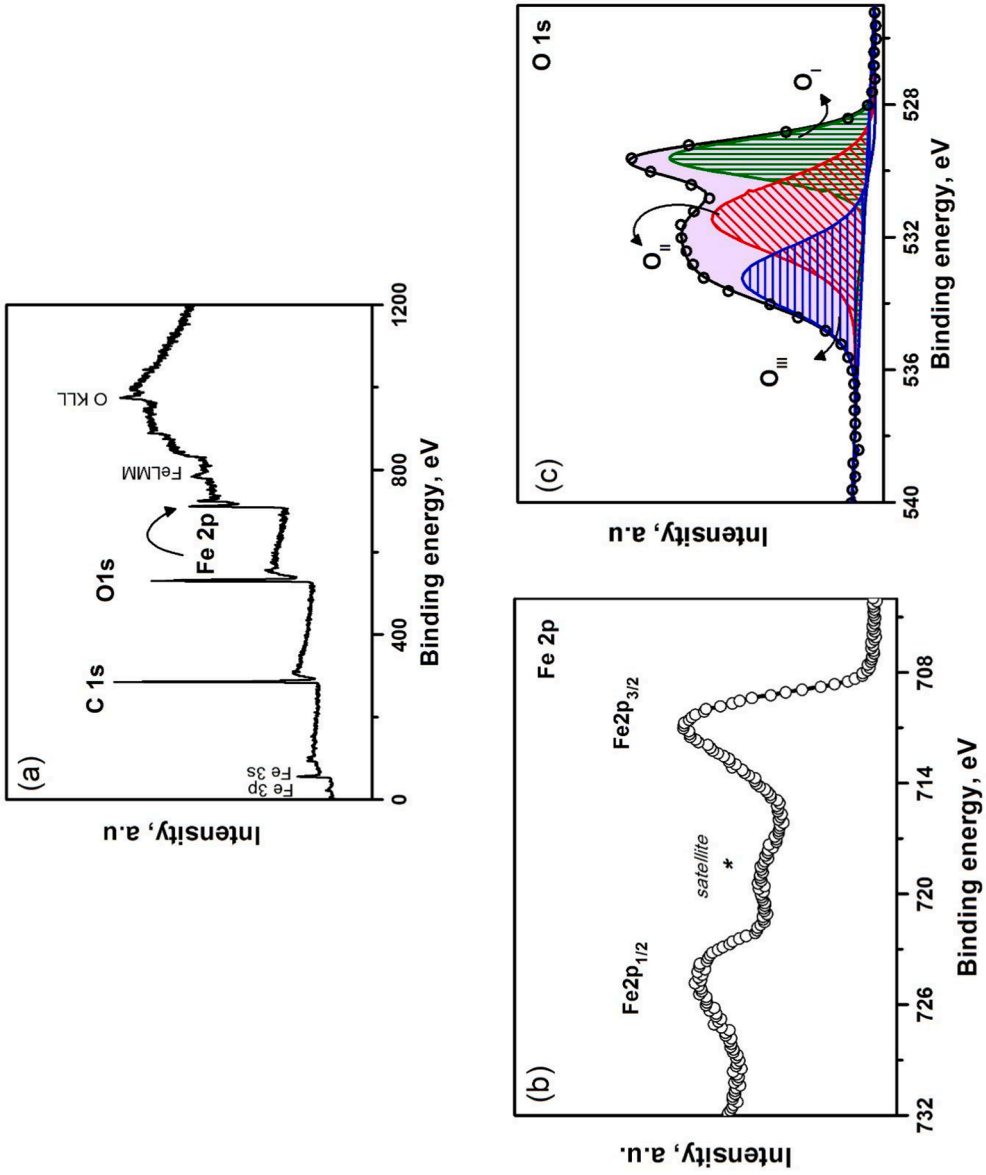

Fig. 3. XPS spectra of α-Fe_2O_3 rhombuses. (a) Survey scan, (b) Fe 2p, and (c) O 1 s.

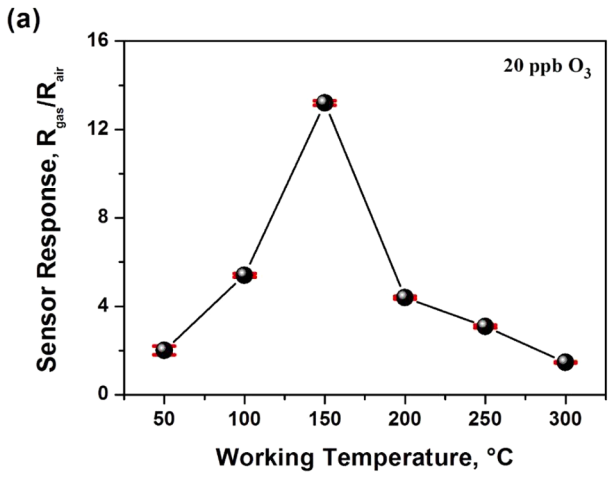

Fig. 4. Gas sensing properties of the α-Fe_2O_3 microrhombuses exposed to 20 ppb O_3 as a function of the operating temperature. (a) Sensor response, and (b) response and recovery times.

Table 1
Summary of results for ozone gas sensors based on several MOXs prepared by different methodologies.

Material	Processing method	Working Temperature (°C)	O_3 concentration (ppb)	Reference
α-Fe_2O_3	RF-Sputtering	200	150	[62]
ZnO	Chemical vapor deposition	200	280	[63]
WO_3	DC - sputtering	250	200	[64]
$Co_xZn_{1-x}O$	Spray pyrolysis	250	20	[65]
WO_3	Vapor phase growth	200	50	[66]
$NiCO_2O_4$	Urea-assisted co-precipitation	200	28	[67]
SnO_2	Spray pyrolysis	200–350	1000	[68]
CuO	RF-Sputtering	200	50	[69]
α-Fe_2O_3	Hydrothermal	150	20	Present study

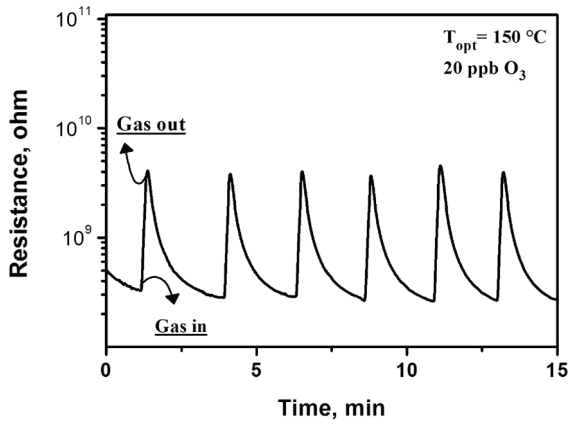

Fig. 5. Dynamic response-recovery curves of α-Fe_2O_3 microrhombuses exposed to 20 ppb of O_3 at 150 °C.

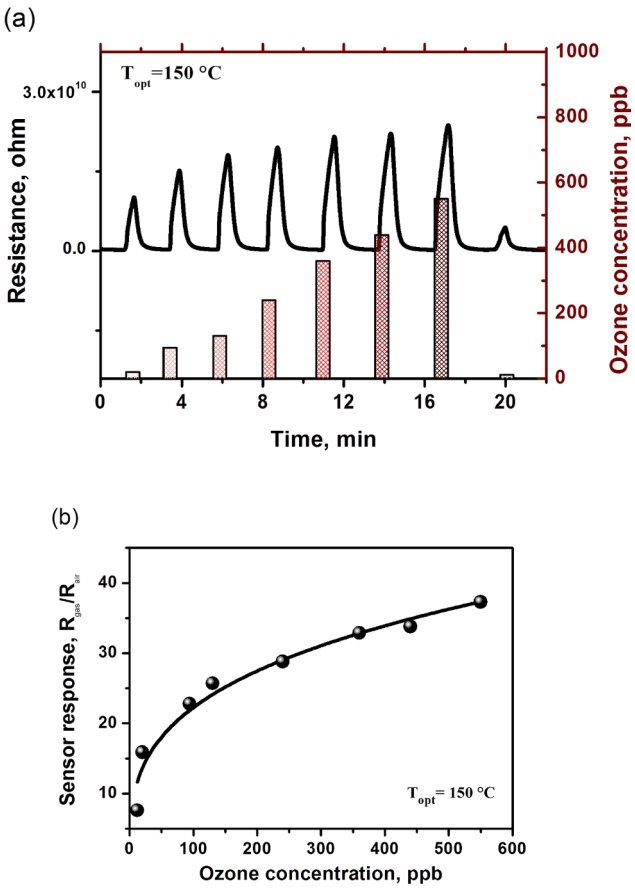

Fig. 6. Rhombus-like shape α-Fe_2O_3 crystals exposed to different O_3 gas levels (12, 20, 94, 130, 240, 360, 440 and 550 ppb) and kept at an operating temperature of 150 °C. (a) Dynamic response-recovery curves, and (b) sensing response versus O_3 gas level.

the presence of O and Fe elements, only. No peak from any impurities can be observed, with the exception of carbon from atmosphere, confirming the efficiency of the synthesis methodology for the obtention of the pristine compound.

Regarding the high-resolution Fe 2p XPS spectrum, Fig. 3**(b)**, we identified two major peaks centered at a binding energy of approximately 710.9 and 724.6 eV corresponding to Fe 2p 3/2 and Fe 2p 1/2 doublet core levels, respectively. Note that such binding energy values are comparable to those reported for Fe^{3+} in the hematite [54–56]. Additionally, the presence of Fe^{3+} species in our sample is confirmed by the shake-up satellite at approximately 719.0 eV [56].

A detailed understanding of chemisorbed oxygen species is believed to be a critical part in the study and development of the chemiresistors. The sensing mechanism has been explained based on interactions

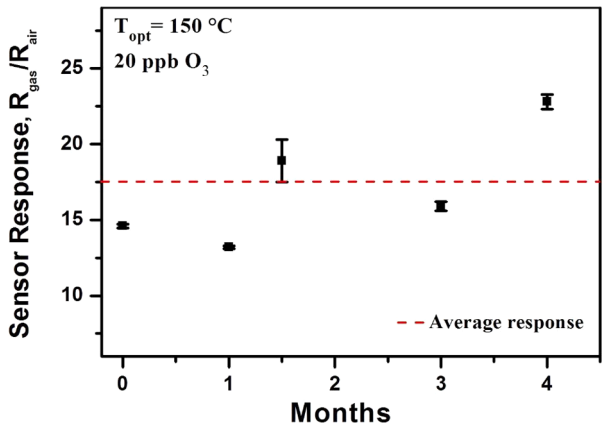

Fig. 7. Long-term stability of rhombus-like α-Fe_2O_3 crystals upon an exposure to 20 ppb of O_3 gas during a period of approximately 4 months.

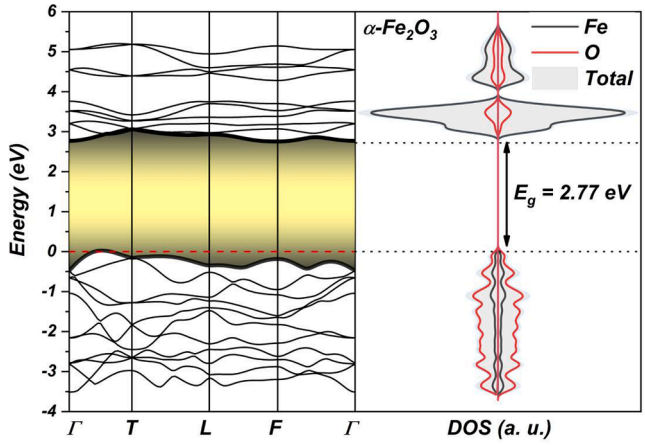

Fig. 8. Atom-resolved DOS profiles and band structures for hematite (α-Fe_2O_3) bulk.

Table 2
Calculated E_{surf}, Fe local coordination, E_{gap} values and O_3 adsorption energies for (0 0 1), (1 0 0), (1 0 1), (1 1 0), (0 1 2), (1 0 4) and (1 1 6) surfaces of α-Fe_2O_3.

Surface	*Area (nm^2)*	*E_{surf} ($J.m^{-2}$)*	*E_{gap} (eV)*	*E_{ads} ($kJ.mol^{-1}$)*	*Fe site*
(0 0 1)	0.226	1.60	2.80	−48.65	Fe_{3c}
(1 0 0)	0.704	1.99	2.84	−219.68	Fe_{4c}
(1 1 0)	0.406	1.58	2.40	−52.08	Fe_{5c}
(1 0 1)	0.246	1.79	2.62	−93.41	Fe_{5c} and Fe_{4c}
(0 1 2)	0.279	1.27	2.83	−165.94	Fe_{5c}
(1 0 4)	0.382	2.11	2.56	−210.02	Fe_{4c}
(1 1 6)	0.608	2.35	2.17	−341.22	Fe_{5c} and Fe_{3c}

between the oxygen species pre-adsorbed on the gas-sensing layer surface [57].

Fig. 3**(c)** displays the high-resolution O 1s spectrum of α-Fe_2O_3 crystals, which was deconvoluted into three components labeled as O_I, O_{II} and O_{III}. From the spectrum analysis, we found that the component O_I centered at 529.6 eV can be linked to the O^{2-} anions present in the hematite lattice. The component O_{II} located at approximately 531.4 eV has been commonly attributed to both hydroxyl groups and/or defective oxygen. The peak at the highest binding energy value (O_{III}) might be due to physisorbed water on metal oxide surfaces [54,56].

3.2. Ozone gas-sensing performance

The ozone gas-sensing properties of the hematite rhombuses were investigated by monitoring the electrical resistance of the sensing layer. It is well-established that the sensing performance of MOX-based gas sensors depends on their working temperature and the analyte level chemisorbed on the MOX surface [58,59].

To find the optimum working temperature (T_{work}), the sensor was submitted to different temperatures, ranging from 50 °C to 300 °C. For each studied temperature, we collected 3 exposure cycles of 30 sec and O_3 level of 20 ppb, as depicted in **Fig. S2**. These results confirm that the hematite rhombuses are sensitive to sub-ppm levels of O_3 gas, presenting total recovery. Furthermore, we observed an increase in the electrical resistance of the sample when exposed to O_3 gas, a typical behavior of n-type sensing layer in an oxidizing environment [17,60].

From data extraction, **Fig. S2**, the tendency of ozone response (S) as function of working temperature (T_{work}) was obtained, Fig. 4**(a)**. As it can be seen, the response of the hematite rhombuses was enhanced by increasing the temperature, reaching a maximum value (S = 13) for a T_{work} around 150 °C. At higher temperatures, the response was significantly lower.

Chemiresistors based on MOXs require a minimum activation energy for the analyte adsorption on the MOX surface, which is usual for sensors thermally activated in a temperature range between 150 and 400 °C. Gas sensors operating at a relatively low temperature have attracted attention due to their less energy consumption and capability of detecting flammable and/or harmful gases. Herein, the α-Fe_2O_3 rhombuses exhibited a maximum response of ca. 13 towards 20 ppb of O_3 at an optimum temperature of 150 °C. It is worth mentioning that the rhombuses were also sensitive to ozone gas at near-room temperature (50 °C), as seen in Fig. 4**(a)**. However, Fig. 4**(b)** reveals that the recovery and response times were also influenced by the operating temperature. Moreover, such time intervals became too long for temperatures lower than 100 °C Thus, it is necessary to obtain an optimum value for the operating temperature to ensure a better match between the equilibrium of the surface reactions, i.e. the occurrence of adsorption and desorption processes within an adequate response and recovery time [17,59,61].

The results presented in Fig. 4**(a)** show a maximum response value at around

150 °C, which is close to that of traditional gas sensors based on MOXs (e.g. WO_3, In_2O_3, and SnO_2) [4]. Table 1 presents a summary of some recent studies reported for ozone gas sensors based on MOXs containing the operating temperature and minimum ozone levels detected. By comparing the results obtained here and those reported in the literature, it is plausible to affirm that α-Fe_2O_3 rhombuses can be considered an excellent gas sensing, even at low ozone concentration (20 ppb) and operating temperature of 150 °C, thus demonstrating their great potential.

Subsequently, the α-Fe_2O_3 microrhombuses were maintained at 150 °C and then tested in consecutive exposure cycles of 20 ppb of O_3 so as to evaluate their response repeatability and surface chemical stability. Fig. 5 shows dynamic response-recovery curves, where it can be observed that the resistance of the microrhombuses increased in the presence of O_3 molecules, a typical behavior of an n-type semiconductor. As it can be seen, the microrhombuses presented complete and fast recovery, which means a stable and reproducible response, indicating that their surface was not poisoned by the repeated sensing tests. Also, the high repeatability of the sensor response was evidenced, confirming the feasibility of the obtained sensing response exhibited by the hematite rhombuses.

The gas-sensing performance of the α-Fe_2O_3 microrhombuses was further investigated by exposing them to a temperature of 150 °C and to

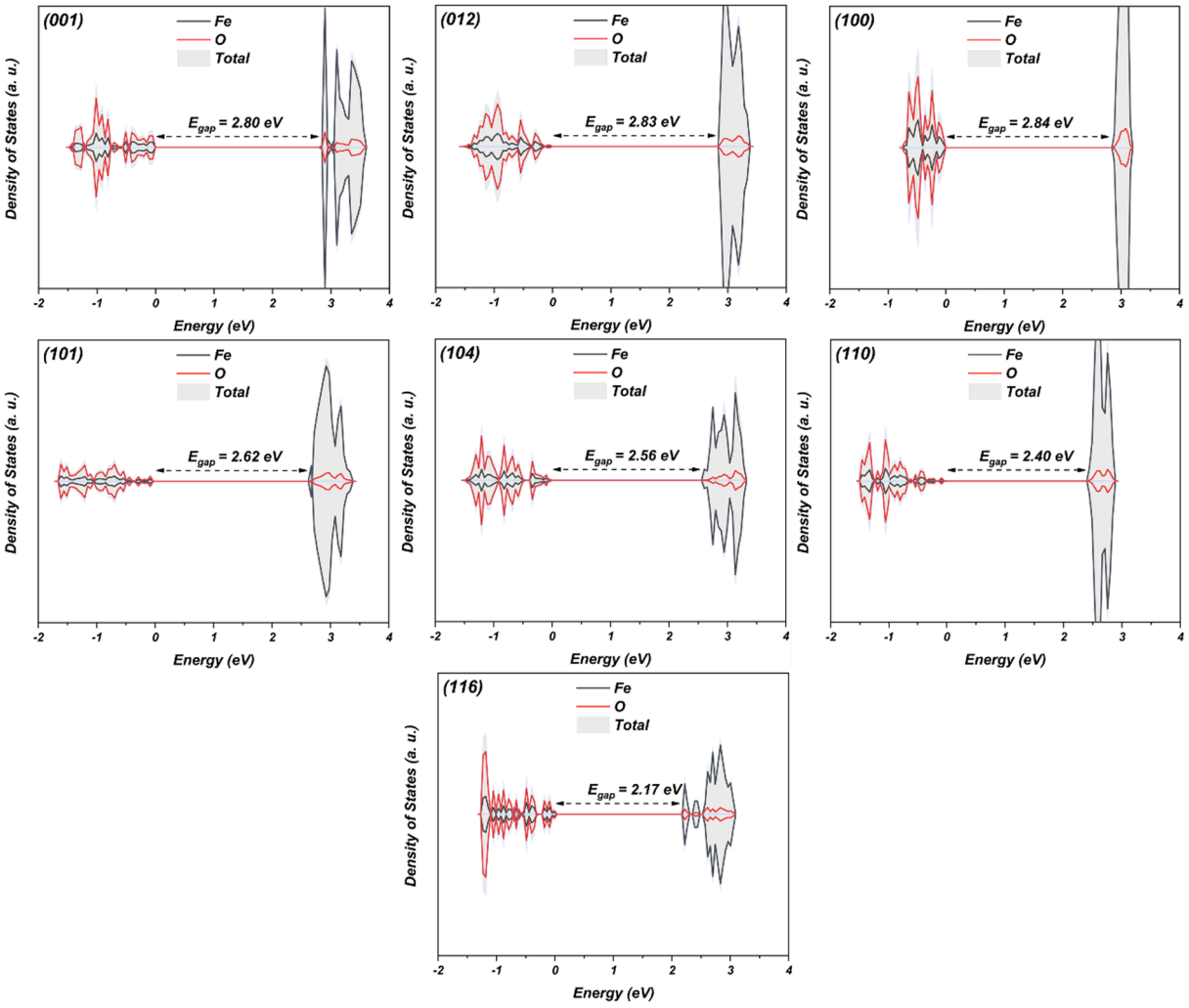

Fig. 9. Atom-resolved density of states profiles for (0 0 1), (1 0 0), (1 0 1), (1 1 0), (0 1 2), (1 0 4) and (1 1 6) surfaces of α-Fe_2O_3.

different O_3 levels in the range of 12 to 550 ppb, Fig. 6. It can be noted that the sensor response (S) increased significantly, reaching a value of approximately S = 37 for 550 ppb of O_3 gas. It is important to mention that the gas sensor based on α-Fe_2O_3 microrhombuses was able to detect ozone concentrations below 20 ppb after the detection of higher ozone levels.

Fig. 6**(b)** shows the variation of the sensor response versus O_3 gas level. An exponential trend in the sensor response of hematite microrhombuses typical of MOXs applied as a sensing layer was obtained.

The long-term stability of the α-Fe_2O_3-based sensors for 20 ppb of O_3 gas at 150 °C is displayed in Fig. 7**.** The result indicates that α-Fe_2O_3 has good stability in natural environment after 4 months. Additionally, it is reasonable to believe that rhombus-like α-Fe_2O_3 crystals can be considered a potential sensing material for practical applications in order to monitor ground-level ozone.

3.3. DFT calculations

First, in order to describe the structural properties of the α-Fe_2O_3 compound, we calculated its respective lattice parameters and bond lengths. The calculated lattice parameters of the hematite yielded the following values: a = 5.107 Å and c = 13.779 Å (V = 311.27 $Å^3$), which are in agreement with the literature [70]. From an inspection of Fig. 1**,** it is possible to observe that the crystalline structure of the hematite is composed of regular prismatic [FeO_6] clusters containing three short/long Fe-O bonds equal to 1.978 Å and 2.117 Å.

The electronic structure of the hematite compound was investigated using DOS projections and band structure profiles, as illustrated in Fig. 8. In this case, the DOS profiles indicate that the valence band (VB) is mainly constituted by oxygen (2*p*) states, while the conduction band (CB) is predominantly formed by empty 3*d* states from Fe. In addition, the band structure profiles indicate an indirect band gap energy of 2.77 eV, starting from an intermediary point between Γ and T (called Y) to Γ in the CB. It is worth mentioning that the theoretical band gap energy was calculated considering optimal conditions; therefore, differences in the experimental value above that mentioned are expected.

From now on, our major interest is devoted to rationalizing the energetic, structural, electronic and morphological properties of the investigated surface models for hematite crystals. Table 2 summarizes the calculated E_{surf} values for each hematite surface, the corresponding Fe coordination number at the exposed surface and its band-gap energy

It can be observed that the stability order of the investigated surfaces of the hematite crystal was found to be: (0 1 2) > (1 1 0) > (0 0 1) > (1 0 1) > (1 0 0) > (1 0 4) > (1 1 6). Such result is in agreement with the undercoordination degree reported in Table 2, i.e., the higher number of dangling bonds along the exposed surface induces a higher E_{surf} values. Regarding the theoretical band-gap energy, all surfaces presented distinct values in comparison to the bulk (Fig. 1), which can be

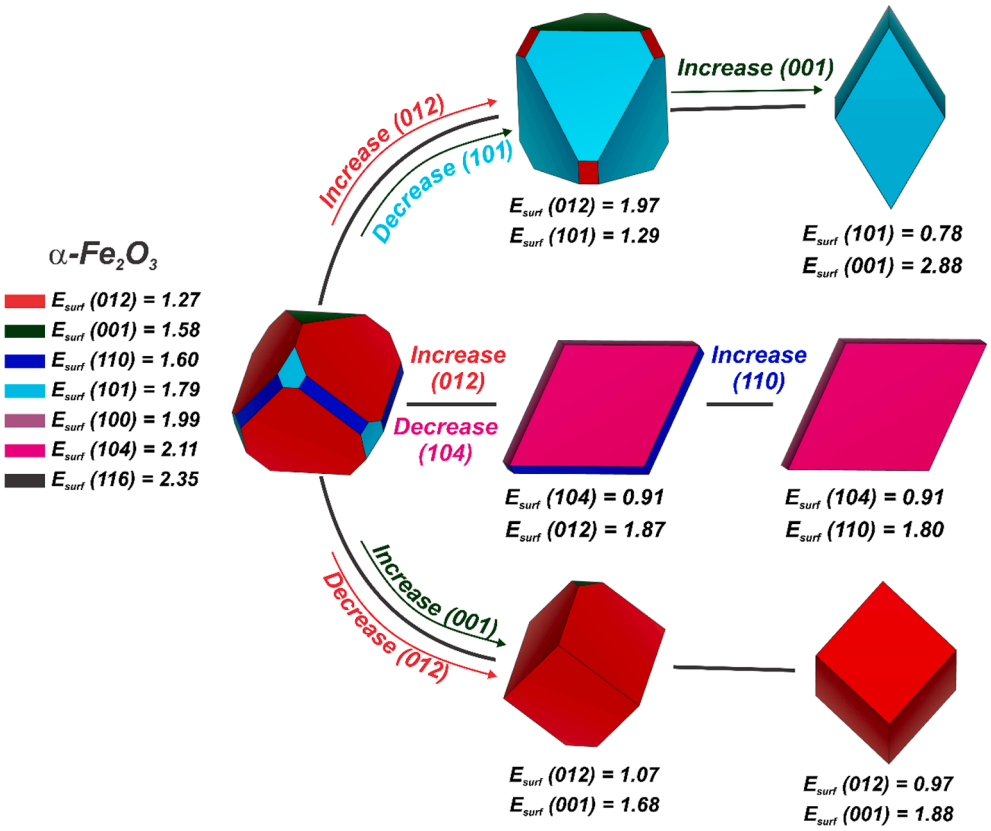

Fig. 10. Theoretical morphologies obtained for α-Fe_2O_3 using Wulff construction. The E_{surf} values are reported in Jm^{-2}.

associated with the singular chemical environment of each exposed surface that perturbs the distribution of energy levels in the vicinity of the band-gap region, Fig. 9.

Aiming to investigate the role of exposed surfaces in the crystal morphology of α-Fe_2O_3, the Wulff Construction was applied considering the optimized E_{surf} values.

Fig. 10 illustrates the Wulff shapes predicted for the α-Fe_2O_3 crystal. Taking into account an ideal vacuum, it can be observed that the morphology of α-Fe_2O_3 is based on corner and side-truncated cubic shape enclosing the (0 1 2), (1 1 0), (0 0 1) and (1 0 1) surfaces. By controlling the E_{surf} values for different α-Fe_2O_3 surfaces, two main types of morphological paths were then found, following the experimental results reported in

Fig. 2 (SEM/TEM images in Section 3.1). In addition, the control of the exposure of (1 0 4), (0 1 2) and (1 0 1) surface planes resulted in three rhombus shapes (regular and non-regular). In the first case, the cubic shape enclosing the (0 1 2) surface plane is regular, while in the other cases the shape enclosing the (1 0 1) or (1 0 4) surface is triclinic.

Aiming to understand the role of α-Fe_2O_3 surfaces in the O_3 sensing properties, adsorption models were calculated. Fig. 11 summarizes the obtained geometries after O_3 adsorption along the (0 0 1), (1 0 0), (1 0 1), (1 1 0), (0 1 2), (1 0 4) and (1 1 6) surfaces.

Table 2 summarizes the adsorption energies (E_{ads}) estimated with B3LYP-D3 level of theory after BSSE correction. The O_3 adsorption energies followed the order (1 1 6) > (1 0 0) > (1 0 4) > (0 1 2) > (1 0 1) > (1 1 0) > (0 0 1). Indeed, the calculated values indicate that (1 1 6), (1 0 0) and (1 0 4) are the most favorable surfaces for O_3, according to the higher dangling bond density along the exposed surfaces. From an inspection of Fig. 11, it was possible to observe that the O_3 adsorption process occur from a two-fold interaction, i.e., two O atoms from the O_3 molecule interact with exposed undercoordinated Fe cations with distances ranging from 1.885 to 2.260 Å. In this case, the adsorption mechanism can be classified as chemisorption due to the creation of new Fe-O bond paths without O_3 bond-breaking mechanism. In an opposite direction, the (1 1 0) and (0 0 1) surfaces showed the smallest values for O_3 adsorption energies as a result of the stable character of exposed Fe centers that induces a one-fold O pointed physical adsorption.

In particular, the adsorption energies calculated for (1 0 4), (0 1 2) and (1 0 1) showed that such surfaces act in a chemisorption process associated with the formation of new Fe-O bond interactions ranging from 1.897 to 2.320 Å, without any bond-breaking mechanism for the O_3 molecule. However, the adsorption process is more favorable at the (1 0 4) surface due to the O_3 interaction with two exposed Fe centers, followed by (0 1 2), where the proximity of exposed undercoordinated Fe centers induces a very reactive center for O_3 adsorption in comparison with (1 0 1), where the geometry distribution of exposed undercoordinated Fe centers reduces the interaction.

Therefore, by combining the O_3 adsorption energies (Table 2) and the morphological modulation depicted in Fig. 11 it was possible to corroborate the experimental measurements for O_3 gas-sensing properties of α-Fe_2O_3 rhombuses, indicating that (1 0 4), (0 1 2), and (1 0 1) surfaces can play a key role in the superior gas-sensing properties. Moreover, the rhombus shape enclosed by (1 0 4) surfaces exhibited the highest sensing performance towards O_3 gas, making shape-oriented α-Fe_2O_3 rhombuses excellent candidates for application as gas sensors.

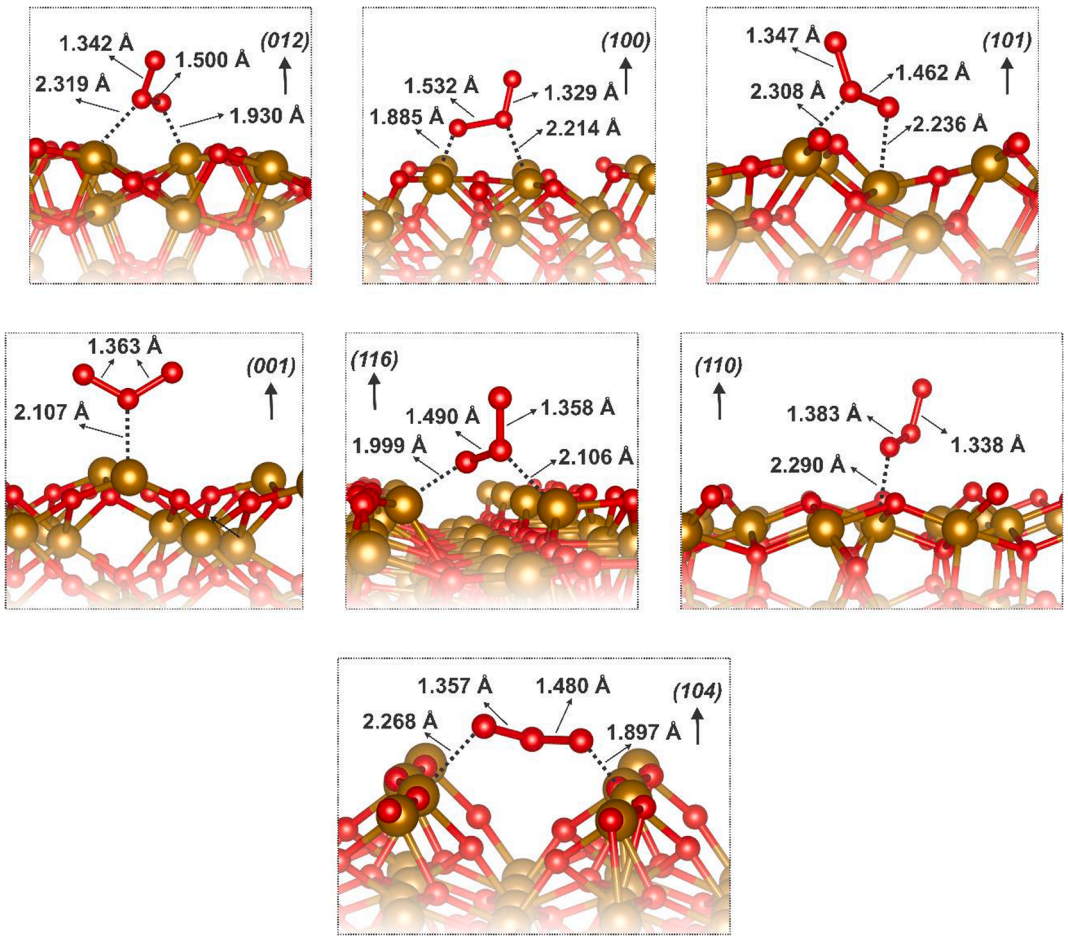

Fig. 11. Optimized geometries for O_3 adsorption along the (0 0 1), (1 0 0), (1 0 1), (1 1 0), (0 1 2), (1 0 4) and (1 1 6) surfaces of α-Fe_2O_3. The Fe-O_3 and O-O bond lengths were depicted to represent the overall reorganization after the adsorption process.

4. Conclusions

In summary, an experimental and theoretical investigation of the ozone-sensing performance of hematite crystals was performed. Experimental results indicated that the as-obtained sample presented a pure hematite phase, exhibiting a morphology based on well-defined rhombus-like shape. Gas-sensing experiments indicated that microrhombuses are sensitive to sub-ppm levels of ozone, being able to detect concentrations ranging from 12 to 550 ppb. In addition, hematite rhombuses also presented complete recovery, good repeatability, and stability for a period superior to 4 months. Computational simulations demonstrated that the (1 0 4), (0 1 2) and (1 0 1) surfaces are favorable to chemisorption processes. However, it was found that the (1 0 4) surface provides a more reactive site for the adsorption of O_3 molecules, confirming that rhombus-oriented α-Fe_2O_3 particles mostly enclosing the (1 0 4) surface plane are mandatory for obtaining superior gas-sensing properties. Our findings confirm the potential of α-Fe_2O_3 microrhombuses as a sensing layer for the detection of sub-ppm levels of O_3, besides demonstrating the importance of exposed surface facets in the adsorption/desorption processes of O_3 molecules.

CRediT authorship contribution statement

Ariadne C. Catto: Conceptualization, Methodology, Data curation, Validation, Writing - original draft, Investigation, Visualization, Writing - review & editing. **Marisa C. Oliveira:** Software, Formal analysis. **Renan A.P. Ribeiro:** Software, Validation, Formal analysis, Writing - review & editing. **Waldir Avansi:** Data curation, Writing - review & editing. **Luís F. Silva:** Conceptualization, Visualization, Resources, Writing - review & editing. **Elson Longo:** Supervision, Writing - review & editing, Funding acquisition.

Declaration of Competing Interest

The authors declare that they have no known competing financial interests or personal relationships that could have appeared to influence the work reported in this paper.

Acknowledgements

We would like to thank Dr. Julio C. Sczancoski for the XRD pattern. Furthermore, this research was partially performed at the Brazilian Nanotechnology National Laboratory (Microfabrication team: Project LMF-18580), Campinas, SP, Brazil. We also thank the Laboratory of Structural Characterization (LCE/ DEMa/UFSCar) for the TEM facilities. The authors acknowledge the financial support of the Brazilian research funding institutions: FAPESP (under grants Nos. 2021/01651-1, 2019/18082-2, 2018/18208-0,2017/12437-5 and 2013/07296-2), CNPq (under grants Nos. 405140/2018-5, 426511/ 2018-2, 308706/2018-8, and 311463/2017-7) and CAPES. M. C. Oliveira acknowledges the financial support from PNPD/CAPES (88887.319041/2019-00). The authors also thank the National Laboratory for Scientific Computing (LNCC) and the High-Performance Computing Center (NACAD) at the Federal University of Rio de Janeiro (COPPE-UFRJ) for providing the computational resources of Lobo Carneiro supercomputer.

Appendix A. Supplementary material

Supplementary data to this article can be found online at https://doi.org/10.1016/j.apsusc.2021.150209.

References

[1] J. Rhee, F. Dominici, A. Zanobetti, J. Schwartz, Y. Wang, Q. Di, J. Balmes, D. C. Christiani, Impact of Long-Term Exposures to Ambient PM2.5 and Ozone on ARDS Risk for Older Adults in the United States, Chest. 156 (1) (2019) 71–79, https://doi.org/10.1016/j.chest.2019.03.017.

[2] M.G. Mustafa, Biochemical basis of ozone toxicity, Free Radic. Biol. Med. 9 (3) (1990) 245–265, https://doi.org/10.1016/0891-5849(90)90035-H.

[3] B. Petracca, B. Rothen-Rutishauser, G. Valacchi, M. Eeman, Bench approaches to study the detrimental cutaneous impact of tropospheric ozone, J. Expo. Sci. Environ. Epidemiol. 31 (1) (2021) 137–148, https://doi.org/10.1038/s41370-020-00275-4.

[4] G. Korotcenkov, V. Brinzari, B.K. Cho, In_2O_3- and SnO_2-Based Thin Film Ozone Sensors: Fundamentals, J. Sensors. 2016 (2016) 1–31, https://doi.org/10.1155/2016/3816094.

[5] G. Korotcenkov, Metal oxides for solid-state gas sensors: What determines our choice? Mater. Sci. Eng. B. 139 (1) (2007) 1–23, https://doi.org/10.1016/j.mseb.2007.01.044.

[6] C. Wang, L. Yin, L. Zhang, D. Xiang, R. Gao, Metal Oxide Gas Sensors: Sensitivity and Influencing Factors, Sensors (Basel). 10 (2010) 2088–2106, https://doi.org/10.3390/s100302088.

[7] A. Ponzoni, C. Baratto, N. Cattabiani, M. Falasconi, V. Galstyan, E. Nunez-Carmona, F. Rigoni, V. Sberveglieri, G. Zambotti, D. Zappa, Metal Oxide Gas Sensors, a Survey of Selectivity Issues Addressed at the SENSOR Lab, Brescia (Italy), Sensors (Basel). 17 (2017) 714, https://doi.org/10.3390/s17040714.

[8] S. Zhao, Y. Shen, R. Maboudian, C. Carraro, C. Han, W. Liu, D. Wei, Facile synthesis of ZnO-SnO_2 hetero-structured nanowires for high-performance NO_2 sensing application, Sensors Actuators B Chem. 333 (2021) 129613, https://doi.org/10.1016/j.snb.2021.129613.

[9] L.F. da Silva, A.C. Catto, S. Bernardini, T. Fiorido, J.V.N. de Palma, W. Avansi, K. Aguir, M. Bendahan, BTEX gas sensor based on hematite microrhombuses, Sensors Actuators B Chem. 326 (2021) 128817, https://doi.org/10.1016/j.snb.2020.128817.

[10] N. Joshi, L.F. da Silva, H.S. Jadhav, F.M. Shimizu, P.H. Suman, J.-C. M'Peko, M. O. Orlandi, J.G. Seo, V.R. Mastelaro, O.N. Oliveira, Yolk-shelled $ZnCo_2O_4$ microspheres: Surface properties and gas sensing application, Sensors Actuators B Chem. 257 (2018) 906–915, https://doi.org/10.1016/j.snb.2017.11.041.

[11] F.K.F. Oliveira, A.A.G. Santiago, A.C. Catto, L.F. da Silva, R.L. Tranquilin, E. Longo, F.V. Motta, M.R.D. Bomio, Cerium molybdate nanocrystals: Microstructural, optical and gas-sensing properties, J. Alloys Compd. 857 (2021) 157562, https://doi.org/10.1016/j.jallcom.2020.157562.

[12] W. Avansi, A.C. Catto, L.F. da Silva, T. Fiorido, S. Bernardini, V.R. Mastelaro, K. Aguir, R. Arenal, One-Dimensional V_2O_5/TiO_2 Heterostructures for Chemiresistive Ozone Sensors, ACS Appl. Nano Mater. 2 (8) (2019) 4756–4764, https://doi.org/10.1021/acsanm.9b00578.

[13] R. Cristina de Oliveira, R.A. Pontes Ribeiro, G.H. Cruvinel, R.A. Ciola Amoresi, M. H. Carvalho, A.J. Aparecido de Oliveira, M. Carvalho de Oliveira, S. Ricardo de Lazaro, L. Fernando da Silva, A.C. Catto, A.Z. Simões, J.R. Sambrano, E. Longo, Role of Surfaces in the Magnetic and Ozone Gas-Sensing Properties of $ZnFe_2O_4$ Nanoparticles: Theoretical and Experimental Insights, ACS Appl, Mater. Interfaces. 13 (3) (2021) 4605–4617, https://doi.org/10.1021/acsami.0c15681.

[14] A.C. Catto, L.F.d. Silva, M.I.B. Bernardi, S. Bernardini, K. Aguir, E. Longo, V. R. Mastelaro, Local Structure and Surface Properties of Co_x $Zn_{1-x}O$ Thin Films for Ozone Gas Sensing, ACS Appl. Mater. Interfaces. 8 (39) (2016) 26066–26072, https://doi.org/10.1021/acsami.6b08589.

[15] L.F. da Silva, J.-C. M'Peko, A.C. Catto, S. Bernardini, V.R. Mastelaro, K. Aguir, C. Ribeiro, E. Longo, UV-enhanced ozone gas sensing response of ZnO-SnO_2 heterojunctions at room temperature, Sensors Actuators B Chem. 240 (2017) 573–579, https://doi.org/10.1016/j.snb.2016.08.158.

[16] A.C. Catto, T. Fiorido, É.L.S. Souza, W. Avansi, J. Andres, K. Aguir, E. Longo, L. S. Cavalcante, L.F. da Silva, Improving the ozone gas-sensing properties of $CuWO_4$ nanoparticles, J. Alloys Compd. 748 (2018) 411–417, https://doi.org/10.1016/j.jallcom.2018.03.104.

[17] A.C. Catto, L.F. da Silva, C. Ribeiro, S. Bernardini, K. Aguir, E. Longo, V. R. Mastelaro, An easy method of preparing ozone gas sensors based on ZnO nanorods, RSC Adv. 5 (25) (2015) 19528–19533, https://doi.org/10.1039/C5RA00581G.

[18] L.F. da Silva, A.C. Catto, W. Avansi, L.S. Cavalcante, J. Andrés, K. Aguir, V. R. Mastelaro, E. Longo, A novel ozone gas sensor based on one-dimensional (1D) α-Ag2WO4 nanostructures, Nanoscale. 6 (8) (2014) 4058–4062, https://doi.org/10.1039/C3NR05837A.

[19] S. Vallejos, N. Pizúrová, I. Gràcia, C. Sotelo-Vazquez, J. Čechal, C. Blackman, I. Parkin, C. Cané, ZnO Rods with Exposed 100 Facets Grown via a Self-Catalyzed Vapor-Solid Mechanism and Their Photocatalytic and Gas Sensing Properties, ACS Appl. Mater. Interfaces. 8 (48) (2016) 33335–33342, https://doi.org/10.1021/acsami.6b12992.

[20] Y.N. Colmenares, W. Correr, B.S. Lima, V.R. Mastelaro, The effect of morphology on the ozone-gas sensing properties of zinc oxide sputtered films, Thin Solid Films. 703 (2020) 137975, https://doi.org/10.1016/j.tsf.2020.137975.

[21] A. Gurlo, Nanosensors: Does Crystal Shape Matter? Small. 6 (19) (2010) 2077–2079, https://doi.org/10.1002/smll.201000680.

[22] J.Y.T. Chan, S.Y. Ang, E.Y. Ye, M. Sullivan, J. Zhang, M. Lin, Heterogeneous photo-Fenton reaction on hematite (α-Fe2O3){104}{,} 113 and 001 surface facets, Phys. Chem. Chem. Phys. 17 (38) (2015) 25333–25341, https://doi.org/10.1039/C5CP03332B.

[23] E. Bykova, L. Dubrovinsky, N. Dubrovinskaia, M. Bykov, C. McCammon, S. V. Ovsyannikov, H.-P. Liermann, I. Kupenko, A.I. Chumakov, R. Rüffer, M. Hanfland, V. Prakapenka, Structural complexity of simple Fe_2O_3 at high pressures and temperatures, Nat. Commun. 7 (2016) 10661, https://doi.org/10.1038/ncomms10661.

[24] H.J. Park, S.Y. Hong, D.H. Chun, S.W. Kang, J.C. Park, D.-S. Lee, A highly susceptive mesoporous hematite microcube architecture for sustainable P-type formaldehyde gas sensors, Sensors Actuators B Chem. 287 (2019) 437–444, https://doi.org/10.1016/j.snb.2019.01.153.

[25] M. Donarelli, R. Milan, F. Rigoni, G. Drera, L. Sangaletti, A. Ponzoni, C. Baratto, G. Sberveglieri, E. Comini, Anomalous gas sensing behaviors to reducing agents of hydrothermally grown α-Fe_2O_3 nanorods, Sensors Actuators B Chem. 273 (2018) 1237–1245, https://doi.org/10.1016/j.snb.2018.07.042.

[26] C.M. Hung, N.D. Hoa, N. Van Duy, N. Van Toan, D.T.T. Le, N. Van Hieu, Synthesis and gas-sensing characteristics of α-Fe_2O_3 hollow balls, J. Sci. Adv. Mater. Devices. 1 (1) (2016) 45–50, https://doi.org/10.1016/j.jsamd.2016.03.003.

[27] A. Umar, A.A. Ibrahim, R. Kumar, H. Albargi, M.A. Alsaiari, F. Ahmed, Cubic shaped hematite (α-Fe2O3) micro-structures composed of stacked nanosheets for rapid ethanol sensor application, Sensors Actuators B Chem. 326 (2021) 128851, https://doi.org/10.1016/j.snb.2020.128851.

[28] R. Joy, Z. Han, K.e. Xu, X. Pan, N. Liao, H. Zhou, DFT investigation of gas sensing characteristics of Au-doped vanadium dioxide, Phys. Lett. A. 384 (32) (2020) 126823, https://doi.org/10.1016/j.physleta.2020.126823.

[29] M. Li, H. Zhu, G. Wei, A. He, Y. Liu, DFT calculation and analysis of the gas sensing mechanism of methoxy propanol on Ag decorated SnO_2 (110) surface, RSC Adv. 9 (61) (2019) 35862–35871, https://doi.org/10.1039/C9RA02958C.

[30] W. Wei, W. Li, L. Wang, High-selective sensitive NH3 gas sensor: A density functional theory study, Sensors Actuators B Chem. 263 (2018) 502–507, https://doi.org/10.1016/j.snb.2018.02.108.

[31] L. Wang, R. Chai, Z. Lou, G. Shen, Highly sensitive hybrid nanofiber-based room-temperature CO sensors: Experiments and density functional theory simulations, Nano Res. 11 (2) (2018) 1029–1037, https://doi.org/10.1007/s12274-017-1718-9.

[32] J. Hays, A. Punnoose, R. Baldner, M.H. Engelhard, J. Peloquin, K.M. Reddy, Relationship between the structural and magnetic properties of Co-doped SnO_2 nanoparticles, Phys. Rev. B. 72 (2005) 75203, https://doi.org/10.1103/PhysRevB.72.075203.

[33] D.A. Mirabella, P.M. Desimone, M.A. Ponce, C.M. Aldao, L.F. da Silva, A.C. Catto, E. Longo, Effects of donor density on power-law response in tin dioxide gas sensors, Sensors Actuators B Chem. 329 (2021) 129253, https://doi.org/10.1016/j.snb.2020.129253.

[34] L.F. da Silva, J.-C. M'Peko, A.C. Catto, S. Bernardini, V.R. Mastelaro, K. Aguir, C. Ribeiro, E. Longo, UV-enhanced ozone gas sensing response of ZnO-SnO_2 heterojunctions at room temperature, Sensors Actuators, B Chem. 240 (2017) 573–579, https://doi.org/10.1016/j.snb.2016.08.158.

[35] S. Grimme, A. Hansen, J.G. Brandenburg, C. Bannwarth, Dispersion-Corrected Mean-Field Electronic Structure Methods, Chem. Rev. 116 (9) (2016) 5105–5154, https://doi.org/10.1021/acs.chemrev.5b00533.

[36] A.D. Becke, Density-functional thermochemistry. III. The role of exact exchange, J. Chem. Phys. 98 (7) (1993) 5648–5652, https://doi.org/10.1063/1.464913.

[37] R. Dovesi, A. Erba, R. Orlando, C.M. Zicovich-Wilson, B. Civalleri, L. Maschio, M. Rérat, S. Casassa, J. Baima, S. Salustro, B. Kirtman, Quantum-mechanical condensed matter simulations with CRYSTAL, WIREs Comput. Mol. Sci. 8 (4) (2018), https://doi.org/10.1002/wcms.1360.

[38] M. Catti, G. Valerio, R. Dovesi, Theoretical study of electronic, magnetic, and structural properties of α-Fe_2O_3 (hematite), Phys. Rev. B. 51 (1995) 7441–7450, https://doi.org/10.1103/PhysRevB.51.7441.

[39] H.J. Monkhorst, J.D. Pack, Special points for Brillouin-zone integrations, Phys. Rev. B. 13 (12) (1976) 5188–5192, https://doi.org/10.1103/PhysRevB.13.5188.

[40] M.S. Kuklin, A.J. Karttunen, Crystal Structure Prediction of Magnetic Transition-Metal Oxides by Using Evolutionary Algorithm and Hybrid DFT Methods, J. Phys. Chem. C. 122 (43) (2018) 24949–24957, https://doi.org/10.1021/acs.jpcc.8b08238.

[41] Y. Meng, X.-W. Liu, M. Bai, W.-P. Guo, D.-B. Cao, Y. Yang, Y.-W. Li, X.-D. Wen, Prediction on morphologies and phase equilibrium diagram of iron oxides nanoparticles, Appl. Surf. Sci. 480 (2019) 478–486, https://doi.org/10.1016/j.apsusc.2019.03.005.

[42] L.E. Daga, B. Civalleri, L. Maschio, Gaussian Basis Sets for Crystalline Solids: All-Purpose Basis Set Libraries vs System-Specific Optimizations, J. Chem. Theory Comput. 16 (4) (2020) 2192–2201, https://doi.org/10.1021/acs.jctc.9b01004.

[43] K. Adhikari, A. Chakrabarty, O. Bouhali, N. Mousseau, C.S. Becquart, F. El-Mellouhi, Benchmarking the performance of plane-wave vs. localized orbital basis set methods in DFT modeling of metal surface: a case study for Fe-(110), J. Comput. Sci. 29 (2018) 163–167, https://doi.org/10.1016/j.jocs.2018.10.008.

[44] XXV. Zur Frage der Geschwindigkeit des Wachsthums und der Auflösung der Krystallflächen , Zeitschrift Für Krist. - Cryst. Mater. . 34 (1901) 449. https://doi.org/10.1524/zkri.1901.34.1.449.

[45] J. Andrés, L. Gracia, A.F. Gouveia, M.M. Ferrer, E. Longo, Effects of surface stability on the morphological transformation of metals and metal oxides as

investigated by first-principles calculations, Nanotechnology. 26 (40) (2015) 405703, https://doi.org/10.1088/0957-4484/26/40/405703.
[46] M.M. Ferrer, A.F. Gouveia, L. Gracia, E. Longo, J. Andrés, A 3D platform for the morphology modulation of materials: first principles calculations on the thermodynamic stability and surface structure of metal oxides: Co_3O_4, α-F_e2_O3, and I_n2_O3, Model. Simul. Mater. Sci. Eng. 24 (2) (2016) 025007, https://doi.org/10.1088/0965-0393/24/2/025007.
[47] R.L. Tranquilin, L.X. Lovisa, C.R.R. Almeida, C.A. Paskocimas, M.S. Li, M. C. Oliveira, L. Gracia, J. Andres, E. Longo, F.V. Motta, M.R.D. Bomio, Understanding the White-Emitting $CaMoO_4$ Co-Doped Eu3+, Tb3+, and Tm3+ Phosphor through Experiment and Computation, J. Phys. Chem. C. 123 (30) (2019) 18536–18550, https://doi.org/10.1021/acs.jpcc.9b04123.
[48] A.A.G. Santiago, R.L. Tranquilin, M.C. Oliveira, R.A.P. Ribeiro, S.R. de Lazaro, M. A. Correa, F. Bohn, E. Longo, F.V. Motta, M.R.D. Bomio, Disclosing the Structural, Electronic, Magnetic, and Morphological Properties of CuMnO2: A Unified Experimental and Theoretical Approach, J. Phys. Chem. C. 124 (9) (2020) 5378–5388, https://doi.org/10.1021/acs.jpcc.0c00198.
[49] R.A.P. Ribeiro, M.C. Oliveira, A.G. de Sousa, M.R.D. Bomio, F.V. Motta, L. Gracia, S.R. de Lazaro, E. Longo, J. Andrés, First principle investigation of the exposed surfaces and morphology of β-$ZnMoO_4$, J. Appl. Phys. 126 (23) (2019) 235301, https://doi.org/10.1063/1.5131260.
[50] N.L. Marana, S.M. Casassa, J.R. Sambrano, Adsorption of NH_3 with Different Coverages on Single-Walled ZnO Nanotube: DFT and QTAIM Study, J. Phys. Chem. C. 121 (14) (2017) 8109–8119, https://doi.org/10.1021/acs.jpcc.6b10396.
[51] S. Vallejos, I. Gràcia, E. Figueras, C. Cané, Nanoscale Heterostructures Based on Fe2O3@WO3-x Nanoneedles and Their Direct Integration into Flexible Transducing Platforms for Toluene Sensing, ACS Appl. Mater. Interfaces. 7 (33) (2015) 18638–18649, https://doi.org/10.1021/acsami.5b05081.
[52] M. Grätzel, Photoelectrochemical cells, Nature. 414 (6861) (2001) 338–344, https://doi.org/10.1038/35104607.
[53] N.T.A. Thu, N.D. Cuong, L.C. Nguyen, D.Q. Khieu, P.C. Nam, N. Van Toan, C. M. Hung, N. Van Hieu, Fe2O3 nanoporous network fabricated from Fe3O4/ reduced graphene oxide for high-performance ethanol gas sensor, Sensors Actuators B Chem. 255 (2018) 3275–3283, https://doi.org/10.1016/j.snb.2017.09.154.
[54] Z. Jakub, F. Kraushofer, M. Bichler, J. Balajka, J. Hulva, J. Pavelec, I. Sokolović, M. Müllner, M. Setvin, M. Schmid, U. Diebold, P. Blaha, G.S. Parkinson, Partially Dissociated Water Dimers at the Water-Hematite Interface, ACS Energy Lett. 4 (2) (2019) 390–396, https://doi.org/10.1021/acsenergylett.8b02324.
[55] T. Yamashita, P. Hayes, Analysis of XPS spectra of Fe2+ and Fe3+ ions in oxide materials, Appl. Surf. Sci. 254 (8) (2008) 2441–2449, https://doi.org/10.1016/j.apsusc.2007.09.063.
[56] J. Wang, N. Zhang, J. Su, L. Guo, α-Fe_2O_3 quantum dots: low-cost synthesis and photocatalytic oxygen evolution capabilities, RSC Adv. 6 (47) (2016) 41060–41066, https://doi.org/10.1039/C6RA04464F.
[57] E. Ciftyürek, B. Šmíd, Z. Li, V. Matolín, K. Schierbaum, Spectroscopic Understanding of SnO_2 and WO_3 Metal Oxide Surfaces with Advanced Synchrotron Based; XPS-UPS and Near Ambient Pressure (NAP) XPS Surface Sensitive Techniques for Gas Sensor Applications under Operational Conditions, Sensors. 19 (21) (2019) 4737, https://doi.org/10.3390/s19214737.
[58] M. Batzill, U. Diebold, Surface studies of gas sensing metal oxides, Phys. Chem. Chem. Phys. 9 (2007) 2307–2318, https://doi.org/10.1039/B617710G.
[59] H. Ji, W. Zeng, Y. Li, Gas sensing mechanisms of metal oxide semiconductors: a focus review, Nanoscale. 11 (47) (2019) 22664–22684, https://doi.org/10.1039/C9NR07699A.
[60] A.C. Catto, L.F.d. Silva, M.I.B. Bernardi, S. Bernardini, K. Aguir, E. Longo, V. R. Mastelaro, Local Structure and Surface Properties of $Co_xZn_{1-x}O$ Thin Films for Ozone Gas Sensing, ACS Appl. Mater. Interfaces. 8 (39) (2016) 26066–26072, https://doi.org/10.1021/acsami.6b08589.
[61] D.R. Miller, S.A. Akbar, P.A. Morris, Nanoscale metal oxide-based heterojunctions for gas sensing: A review, Sensors Actuators B Chem. 204 (2014) 250–272, https://doi.org/10.1016/j.snb.2014.07.074.
[62] M. Debliquy, C. Baroni, A. Boudiba, J.-M. Tulliani, M. Olivier, C. Zhang, Sensing characteristics of hematite and barium oxide doped hematite films towards ozone and nitrogen dioxide, Procedia Eng. 25 (2011) 219–222, https://doi.org/10.1016/j.proeng.2011.12.054.
[63] D. Barreca, D. Bekermann, E. Comini, A. Devi, R.A. Fischer, A. Gasparotto, C. Maccato, C. Sada, G. Sberveglieri, E. Tondello, Urchin-like ZnO nanorod arrays for gas sensing applications, CrystEngComm. 12 (2010) 3419–3421, https://doi.org/10.1039/C0CE00139B.
[64] X. Xu, M. Arab Pour Yazdi, J.-B. Sanchez, A. Billard, F. Berger, N. Martin, Exploiting the dodecane and ozone sensing capabilities of nanostructured tungsten oxide films, Sensors Actuators B Chem. 266 (2018) 773–783, https://doi.org/10.1016/j.snb.2018.03.190.
[65] Y.J. Onofre, A.C. Catto, S. Bernardini, T. Fiorido, K. Aguir, E. Longo, V. R. Mastelaro, L.F. da Silva, M.P.F. de Godoy, Highly selective ozone gas sensor based on nanocrystalline $Zn_{0.95}Co_{0.05}O$ thin film obtained via spray pyrolysis technique, Appl. Surf. Sci. 478 (2019) 347–354, https://doi.org/10.1016/j.apsusc.2019.01.197.
[66] N. Kaur, D. Zappa, N. Poli, E. Comini, Integration of VLS-Grown WO3 Nanowires into Sensing Devices for the Detection of H_2S and O_3, ACS Omega. 4 (15) (2019) 16336–16343, https://doi.org/10.1021/acsomega.9b01792.
[67] N. Joshi, L.F. da Silva, H. Jadhav, J.-C. M'Peko, B.B. Millan Torres, K. Aguir, V. R. Mastelaro, O.N. Oliveira, One-step approach for preparing ozone gas sensors based on hierarchical $NiCo_2O_4$ structures, RSC Adv. 6 (95) (2016) 92655–92662, https://doi.org/10.1039/C6RA18384K.
[68] G. Korotcenkov, B.K. Cho, Ozone measuring: What can limit application of SnO_2-based conductometric gas sensors? Sensors Actuators B Chem. 161 (1) (2012) 28–44, https://doi.org/10.1016/j.snb.2011.12.003.
[69] A. Bejaoui, J. Guerin, J.A. Zapien, K. Aguir, Theoretical and experimental study of the response of CuO gas sensor under ozone, Sensors Actuators B Chem. 190 (2014) 8–15, https://doi.org/10.1016/j.snb.2013.06.084.
[70] I. Ahamed, N. Seriani, R. Gebauer, A. Kashyap, Heterostructures of ε-Fe_2O_3 and α-Fe_2O_3: insights from density functional theory, RSC Adv. 10 (46) (2020) 27474–27480, https://doi.org/10.1039/D0RA04020G.